Journal of Innovative Optical Health Sciences
Vol. 10, No. 5 (2017) 1743007 (10 pages)

DOI: 10.1142/S1793545817430076

Interpreting the biochemical specificity of mouse spinal cord by confocal raman microspectral imaging

Yuze Gong[*,†], Zhuowen Liang[‡], Yaning Yin[*,†], Jiwei Song[‡], Xueyu Hu[‡], Kaige Wang[†], Qingli He[*], Zhe Wang[‡], Jintao Bai[*,†] and Shuang Wang[*,§]

[*]*Institute of Photonics and Photon-Technology*
The Cultivation Base of the State Key Laboratory of
Optoelectronic Technology and Functional Materials
Co-constructed by Ministry of Education
and Shaanxi Province, Northwest University Xi'an
Shaanxi, P. R. China

[†]*Department of Physics, Northwest University*
Xi'an, Shaanxi, P. R. China

[‡]*Department of Orthopaedics, Xijing Hospital*
Fourth Military Medical University
Xi'an, Shaanxi, P. R. China
[§]*wsnwuphy@163.com*

Received 12 August 2017
Accepted 11 September 2017
Published 25 September 2017

Interpreting the biochemical specificity of spinal cord tissue is the essential requirement for understanding the biochemical mechanisms during spinal-cord-related pathological course. In this work, a longitudinal study was implemented to reveal a precise linkage between the spectral features and the molecular composition in *ex vivo* mouse spinal cord tissue by microspectral Raman imaging. It was testified that lipid-rich white matter could be distinguished from gray matter not only by the lipid Raman peaks at 1064, 1300, 1445 and 1660 cm^{-1}, but also by protein (1250 and 1328 cm^{-1}) and saccharides (913 and 1137 cm^{-1}) distributions. *K*-means cluster analysis was further applied to visualize the morphological basis of spinal cord tissue by chemical components and their distribution patterns. Two-dimensional chemical images were then generated to visualize the contrast between two different tissue types by integrating the intensities of the featured Raman bands. All the obtained results illustrated the biochemical characteristics of spinal cord tissue, as well as some specific substance variances between different tissue types, which formed a solid basis for the molecular investigation of spinal cord pathological alterations.

Keywords: Confocal Raman imaging; spinal cord; uni- and multivariate analysis.

[§]Corresponding author.

1. Introduction

Spinal cord carries sensory information from the body and some from the head to the central nervous system via afferent fibers and performs the initial processing of this information.[1] It can not only accomplish a lot of voluntary reflection events by itself, but also mediate involuntary reflexes from brain. Among all the reflection activities, the control of the motor function is the most significant, including adjusting the muscle tension, coordination of muscle activity and maintaining posture action. Similar cross-sectional structures could be observed at all spinal cord levels. A ridge-shaped mass of gray matter in the spinal cord is shaped like a butterfly in the center of the cord and consists of cell bodies of interneurons, motor neurons, neuroglia cells and unmyelinated axons.[2] The white matter is located outside of gray matter and consists almost totally myelinated motor and sensory axons.[3]

Raman spectroscopy (RS) is a noninvasive and inelastic scattering technique which can detect the structural characterizations of substances on the molecular level. As one of Raman-based imaging mechanisms, confocal Raman microspectral imaging (CRMI) provides a high-contrast and high-resolution imaging of molecular composition and structure without introducing any external lables.[4,5] By a commonly used point scanning methodology, hyperspectral datasets could be acquired in multi-dimension, including the spatial coordinates of the point where the spectrum was recorded, the spectral position in wavenumber (cm^{-1}), the spectral intensity (CCD counts) and the relevant time. Uni- and multivariate analyses are usually applied to regenerate typical Raman images by determining the value of each pixel. The primary difference is that one spectrum at a time is evaluated for the univariate analysis and used for the generation of one data point per resulting image.[6] Whereas multivariate analysis uses the information of the entire hyperspectral dataset for the value of each pixel. The chemical and architectural nature could be visualized when the discrete spectroscopic information was obtained from a defined spatial area within an unprocessed sample. Therefore, RS has been applied to investigate the histological features of spinal cord tissue and devastating events such as spinal cord injury (SCI). Recently, Saxena *et al.* explored the possibility of using RS to study demyelination and chondroitin sulfate proteoglycans upregulation after SCI.[7] Ruberto *et al.* demonstrated that Raman spectra of an SCI can be observed using an organotypic model.[8] Galli *et al.* assessed the ability of Fourier transform infrared spectroscopy and spontaneous RS to generate contrast data between normal and altered regions on the molecular level in an SCI rat model.[9] They also applied RS for the characterization of morphochemical properties of surgically induced SCI in the rat that received an implant of soft unfunctionalized alginate hydrogel.[10] Besides that, coherent anti-Stokes RS was also used for visualization of myelin sheets in normal spinal cord and for study of myelin sheet swelling and myelin sheet retraction and repair after SCI.[9,11]

In this work, a spectral assessment of spinal cord tissue was achieved on longitudinal tissue sections from healthy mice. The acquired spectral information addressed biochemical characteristics of white and gray matter, as well as some specific substance variances between them. By visualizing lipid, protein and saccharides distributions, the achieved results clearly exhibit heterogeneous biochemical constitution in mouse spinal cord tissue, which provides a solid foundation for the study on the pathobiological characteristics of SCI and its therapeutic mechanisms.

2. Experimental

2.1. *Sample preparation*

The mice were perfusion fixed using 4% paraformaldehyde in phosphate-buffered saline. The T9 spinal cord segments of mice were removed and post-fixed in paraformaldehyde for 24 h at 4°C for *ex vivo* investigations. The spinal cords from six mice were cut into totally 18 pieces for tissue sectioning. Dehydration in rising sucrose concentration (10% for 24 h and 30% for 24 h) was followed by embedding the isolated spinal cords in tissue freezing medium. Samples were snap frozen on liquid nitrogen and stored at −80°C. Longitudinal tissue sections of 20 μm thickness were prepared on gold-coated slides for spectroscopic analysis (BioGold® 63479-AS, Electron Microscopy Sciences, USA), which is used to eliminate the background fluorescence from the microscope slides and optics for spectroscopic measurement. Consecutive sections of 5 μm thickness were prepared on glass slides and hematoxylin and eosin (H&E) stained to provide

direct comparison of the spectroscopic imaging results to histopathology. In addition, a schematic of the hemisection surgery of the mice model is shown in Fig. S-1 (available in Supplementary Information). The sections were stored at −20°C until use and allowed to thaw for 30 min prior to spectroscopic analysis or further histological processing.

2.2. *Confocal Raman microspectroscopy*

The Raman spectra were acquired with an Alpha 500R confocal Raman microspectroscopy (WITec GmbH, Germany) equipped with a helium-neon 633 nm (35 mW@633 nm, Research Electro-optics, Inc., USA) excitation laser and a piezo scanning table for image scanning. A 100 μm diameter optical fiber is used to be the optical coupling between microscope and spectrometer. With a 633 nm holographical beam splitter, the laser beam is coupled into a 20 × objective (NA = 0.5, Epiplan-Neofluar, Zeiss, Germany) or a 63 × objective (NA = 0.85, N-Achroplan, Zeiss, Germany). The scanning movement of the sample is performed by a multi-axis piezo scanning stage (P-524K081, PI GmbH, Germany), which has a 150 × 100 mm travel range, 3 μm resolution, 100 nm step-width and 3 μm positioning accuracy. The Raman scattering photons were collected by the same objective lens and then sent into a 50 μm diameter optical fiber through a holographic edge filter. The spectral signal was monitored by a spectrometer (UHTS300, WITec GmbH, Germany) incorporating a 600 mm^{-1} grating blazed at 500 nm with a resolution of approximately 3 cm^{-1} over the range 0–3000 cm^{-1}. The Raman spectrum was recorded by a back-illuminated deep-depletion charge coupled device (CCD) camera (Du401A-BR-DD-352, Andor Technology, UK) working at −60°C. The spectral datasets were continuously scanned point-by-point over every measuring point on the *xy* plane. Each spectrum was accumulated at a speed of 1 s/pixel. The wavelength was calibrated using the Raman scattering peak of Si at 521 cm^{-1}, and the spectral

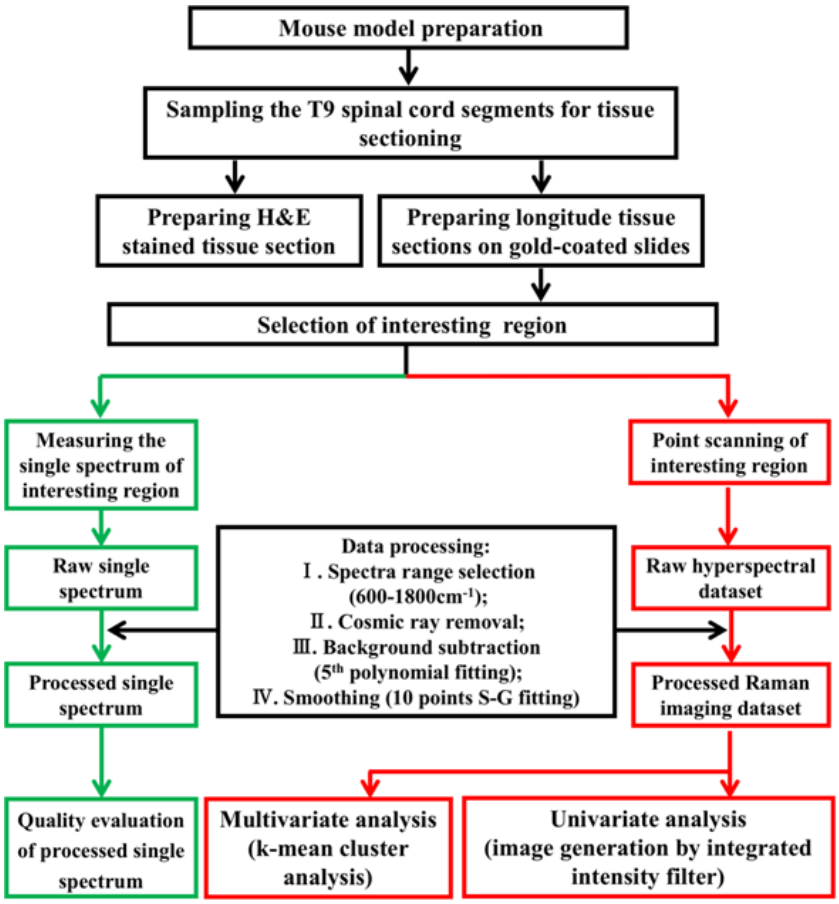

Fig. 1. A flowchart of all experimental steps used to analyze spectral information about mouse spinal cord tissue.

response of the system was calibrated using an NIST traceable tungsten calibration lamp (RS-3, EG&G Gamma Scientific, USA).

2.3. *Data analysis*

WITec Project FOUR (WITec GmbH, Germany) was utilized to preprocess the acquired dataset shown in Fig. 1. The main steps are as follows: (1) spectral range selection; (2) cosmic ray removal; (3) background subtraction with 5 order polynomial fitting; (4) 10 points Savitzky–Golay (SG) smoothing. After that, a four-dimensional dataset, which is in two directions of the scanning plane (x and y), Raman shift and spectrum intensity, was ready for the image generation. After interpreting the spectral features from 600 to 1800 cm^{-1}, both uni- and multi-variate analyses were adopted to extract composition information of the sample. K-means cluster analysis, one type of multivariate analysis algorithms, was used for automatic identification and visualization of chemical components. Once the number of clusters (N) is defined for the analysis, the algorithm first defines N centers in the 1600 dimensional space and assigns each point (spectrum) the center closest to it. Then, the centroid (one might also call it an average spectrum) for each group is computed. After that, the spectra are again sorted according to their distance to the calculated centroids and then the procedure is repeated. The algorithm is typically stopped once the assignment of the points (spectra) to their group ceases to change.[12] The cluster membership information was plotted as a color-coded image, and the average spectrum of each cluster was used to detect variations in Raman band position and/or intensity among the different regions. To access the micro-distribution of a certain biochemical composition, univariate analyses were performed to evaluate the integrated intensity of specific peaks within the scanning area.

3. Results and Discussion

3.1. *Spectral features of mouse spinal cord tissue*

Histologically, white and gray matter consists of varying types of nerve and glial cells, strictly aligned long nerve fibers and fiber tracts, endothelial cell and vessels,[3] as shown in the microphotograph of a longitudinal H&E-stained spinal cord section (Fig. 2(a)). Even in the absence of staining as shown in Fig. 2(b), the five main layers can be easily distinguished that gray matter in a darker color distributed in the middle of two bright white matter layers. The white matter consists almost totally of white myelinated axons,[13] exhibiting a condensed filamentary structure on the right of Fig. 2(c); whereas gray matter, which contains more nerve cell bodies, presents a reticular structure on the left.

After spectral data preprocessing, the pure Raman spectra of the spinal cord sample were smoothed and normalized to their respective area under curve, as shown in Fig. 2(d). Although the captured data were averaged over many measuring spots, some consistent systematic characteristics could be identified. Putative peak assignments, listed in Table 1, were summarized based on the literature related to RS of human brain, human spinal cord and mouse spinal cord.[7,9,10,14–16] The Raman spectra were characterized by intense bands at 750, 875, 913, 1003, 1064, 1137, 1250, 1300, 1328, 1445, 1578 and 1660 cm^{-1}. Certain lipid spectral features, such as 1064 cm^{-1}(C–C stretching), 1300 cm^{-1}(CH_2 twisting and wagging), 1445 cm^{-1}(CH_2 bending/scissoring) and 1660 cm^{-1} (amide I/(C=O) stretching), were very apparent in Fig. 2(d). Furthermore, a prominent spectral feature in white matter is that its relative lipid band intensity is higher than that of gray matter due to more myelinated axons constitutions.[9] The other spectral feature of white matter at 875 cm^{-1} is the symmetric and antisymmetric stretch vibrations of the choline group N^+ $(CH_3)_3$ in phosphatidylcholine, which is essential for fat metabolism and functions as a methyl donor.[14] Besides lipid peaks, the Raman spectrum of gray matter contains more ingredients at 750, 913, 1003, 1137, 1250, 1328 and 1578 cm^{-1}. Both 750 and 1578 cm^{-1} peaks are strong Raman spectral features of free unconfined heme,[7,17] which is attributed to υ (pyr breathing) and the vibrations of υ_{as} ($C_\alpha C_\beta$). The 913 and 1137 cm^{-1} Raman peaks are attributed to vibrations of the saccharides, as well as vibrations of C-H and C-OH bonds.[7–9] Besides providing protection and lubrication for the spinal cord, saccharides are the skeleton of nerve cells in gray matter.[18] Strong vibrations are also evident in regions assigned to protein (1250 and 1328 cm^{-1}), namely, to the vibrations of amide III and C-H bonds. Phenylalanine, observed at 1003 cm^{-1} Raman peak, is one of

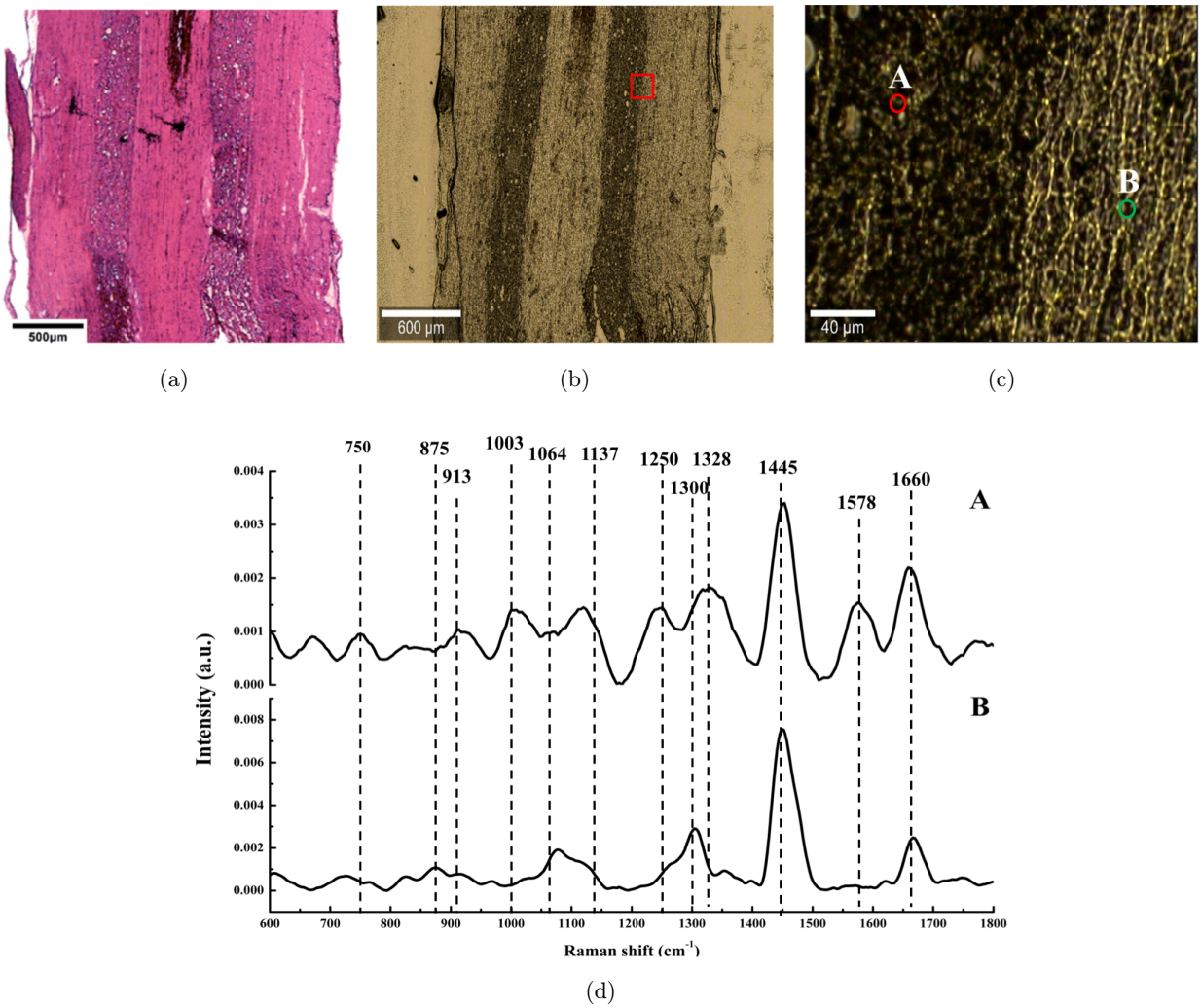

Fig. 2. The microphotograph of a longitudinal H&E-stained spinal cord section with 500 μm scale bar (a); a stitched bright-field microscopy image of the longitudinal section in $3 \times 2\,\text{mm}^2$ with 600 μm scale bar (b); a microscopic image with 40 μm scale bar (c) and the normalized spectra from both gray and white matter (d). The red square in (b) is the localization where the microscopic image (c) recorded. And the green and red circles in image (c) are the spectra acquiring points.

Table 1. Band position and assignments of selected Raman peaks from mouse spinal cord tissue from 600 to 1800 cm^{-1}.

Peak position (cm^{-1})	Assignments	Chemical compounds	References
643	δ(C–C) twisting, C–S	Tyrosine	8, 20, 33
700	Sterol ring	Cholesterol	7–10, 14, 33
750	Υ(pyr breathing); υ_{as} ($C_\alpha C_\beta$)	Heme	17
875	$\upsilon_1(N^+(CH_3)_3)$ and $\upsilon_1(N^+(CH_3)_3)$ stretching	Choline in phosphatidylcholine	14, 33
913	C-OH	Saccharides	8, 20, 33
1003	υ_s (C–C) breathing	Phenylalanine	8–10, 33
1064	υ (C–C) stretching	Lipids	7–10, 14, 33
1137	C–H, C–OH	Saccharides	7–9, 17
1250	Amide III (random coil)	Protein	10, 15, 19, 33
1300	$\delta(CH_2)$ twisting	Lipids	7–10, 14, 17, 33
1328	CH	Protein	19, 21
1445	δ (CH_2) bending/scissoring	Lipids	7–10, 14, 17
1578	υ (pyr breathing); $\upsilon_{as}(C_\alpha C_\beta)$	Heme	7, 17
1660	Amide I/υ (C=O) stretching	Protein or lipids	7–10, 14, 17, 19, 33

the common amino acids used to form proteins, which normally converts to tyrosine featured at 643 cm^{-1} band.[19,20]

3.2. *Raman spectral imaging of mouse spinal cord tissue*

After the analysis on the featured spectra of sample, the ultimate attention was paid to obtain a detailed insight onto its histological features with biochemical substance distributions. To overview the chemical nature of the prepared sample, a $2250 \times 60\,\mu m^2$ area was point scanned with 1 s/pixel integration time and 225×6 pixels. After scanning, a four-dimensional dataset (x, y, Raman shift, Raman intensity) was ready for imaging generation. Since K-means cluster analysis can handle large amounts of data obtained during spectra scanning,[10,12] it was performed to group spectra that have resembling spectral features. After the spectral dataset was imported into the K-means algorithm, the results varied for the number of the clusters (N) and the spectral range, which contained the main peaks of the sample. The result of K-means cluster analysis is shown in Fig. 3 with $N = 5$ which was confirmed by the H&E image in Fig. 3(a). Each cluster was assigned in a pseudocolor Raman image shown in Fig. 3(c). Transformation of it with its corresponding microscopic image (Fig. 3(b)) revealed the morphological origin of the spectra in the sampling area (Fig. 3(d)). The average spectrum of each cluster, shown in Fig. 3(e), illustrated that the green cluster specified with a higher intensity of the lipids bands at 1064, 1300, 1445 and 1660 cm^{-1}; meanwhile, the brown cluster contains more other ingredients inside the sample, such as amide III (1250, 1328 cm^{-1}), heme (750, 1578 cm^{-1}), saccharides (913, 1137 cm^{-1}) and phenylalanine (1003 cm^{-1}).[21] Consistent with the spectral investigation, the brown region with more ingredients represents the gray matter and the green region with higher content of lipids represents the white matter. The spectrum of blue cluster contains the similar intensity of lipid compared with the white matter and the lower intensity of special ingredients of gray matter, which represents a contact region between white and gray matter. Because of the central artery locating in the sampled area (as shown in Fig. S1), some unconfined heme remains in the center of white matter (red area), which can be classified by the highest intensity of 1578 cm^{-1} peak in the spectrum of the red cluster.[22,23] Since the intensity of spectra in cyan area reached to zero, also is the lowest among all five clusters, it means that the cyan area stands for the slides substances.

For a better understanding on tissue chemical make-up, some univariate Raman images are reconstructed from selected Raman bands of each single spectrum obtained from every scanning point in $80 \times 60\,\mu m^2$ with 80×60 pixels. Figure 4 shows the two-dimensional distribution of major biochemical components based on the integration of their marker bands, as well as the combined image of different components. Lipid distribution was visualized by integrating over 1440–1450 cm^{-1} originated from CH_2 bending and scissoring mode.[24,25] The regenerated lipid image exhibited a sequential reduction in the lipid intensity from left to right in Fig. 4(b), which illustrated an edge between gray and white matter due to the decreasing content of axons. The axons in the central nervous system are generally myelinated.[26,27] The myelin is formed by wrapped oligodendroglia cell membranes and contains $\sim 70\%$ lipid and 30% protein by weight.[26,28] Therefore, the obtained Raman image successfully descried the biochemical profile of myelin lipids within spinal cord tissue. Furthermore, investigation on the peak intensity of the lipid band would visually reveal the distribution pattern of myelinated axons, as well as the pathological change of the axon after SCI.

As shown in Fig. 4, tissue microstructure could be identified by the generated lipid image. However, it is still not possible to determine the chemical nature of low-lipid areas. Raman images of protein (1250 cm^{-1}), saccharides (913 cm^{-1}) and tyrosine (643 cm^{-1}) were reconstructed by integration of their featured bands presented in Figs. 4(c)–4(e), respectively. A successive decrease in the intensity of nonlipid signals (i.e., from protein and saccharides) was observed in the areas closed to the gray–white matter boundary. Nevertheless, the boundary between white and gray matter could not be clearly identified, unless a combination image of protein and lipid was generated as shown in Fig. 4(f). As one of main substances forming a neuron cell, proteins are actively involved in fundamental cellular functions in gray matter. Meanwhile, its spatial distribution coincides partially with saccharides, which can be observed in Fig. 4(g). Their overlapping localization suggested that an interaction

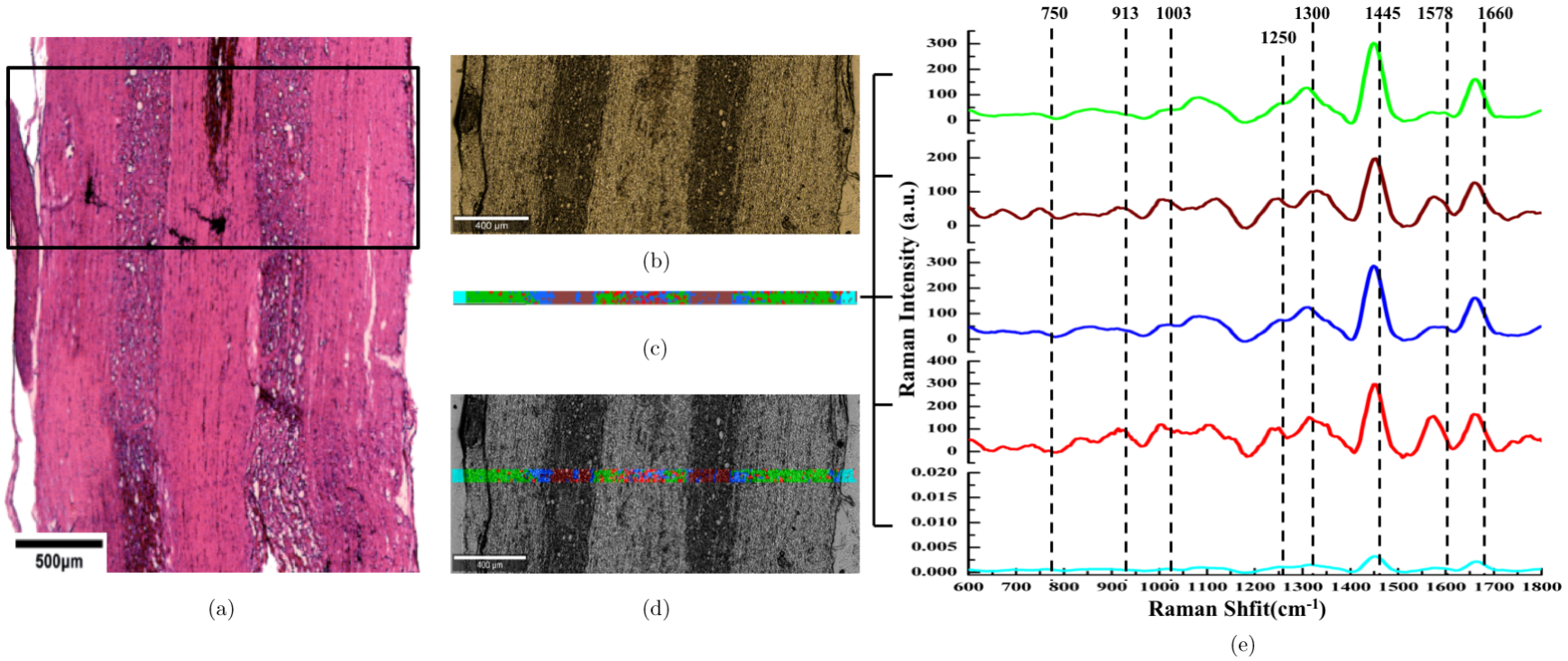

Fig. 3. K-means cluster analysis of *ex vivo* mouse spinal cord tissue sample. The microphotograph of a longitudinal H&E-stained spinal cord section in $2.25 \times 3\,\text{mm}^2$ with $500\,\mu$m scale bar (a); the large area bright-field microscopy image in $2.25 \times 1\,\text{mm}^2$ with $400\,\mu$m scale bar (b); the spectral image (c) was obtained by K-means cluster analysis; The transformed image between (b) and (c) was represented in (d) with $400\,\mu$m scale bar. The black square in (a) is the localization where the microscopic image (b) was recorded. The mean spectra of each sub-cluster are shown on the right (e), which includes white (green) and gray (brown) matter, contact region (blue) between gray and white matter, the unconfined heme (red), as well as the glass slide (cyan). The images (b), (c) and (d) are all with $400\,\mu$m scale bar.

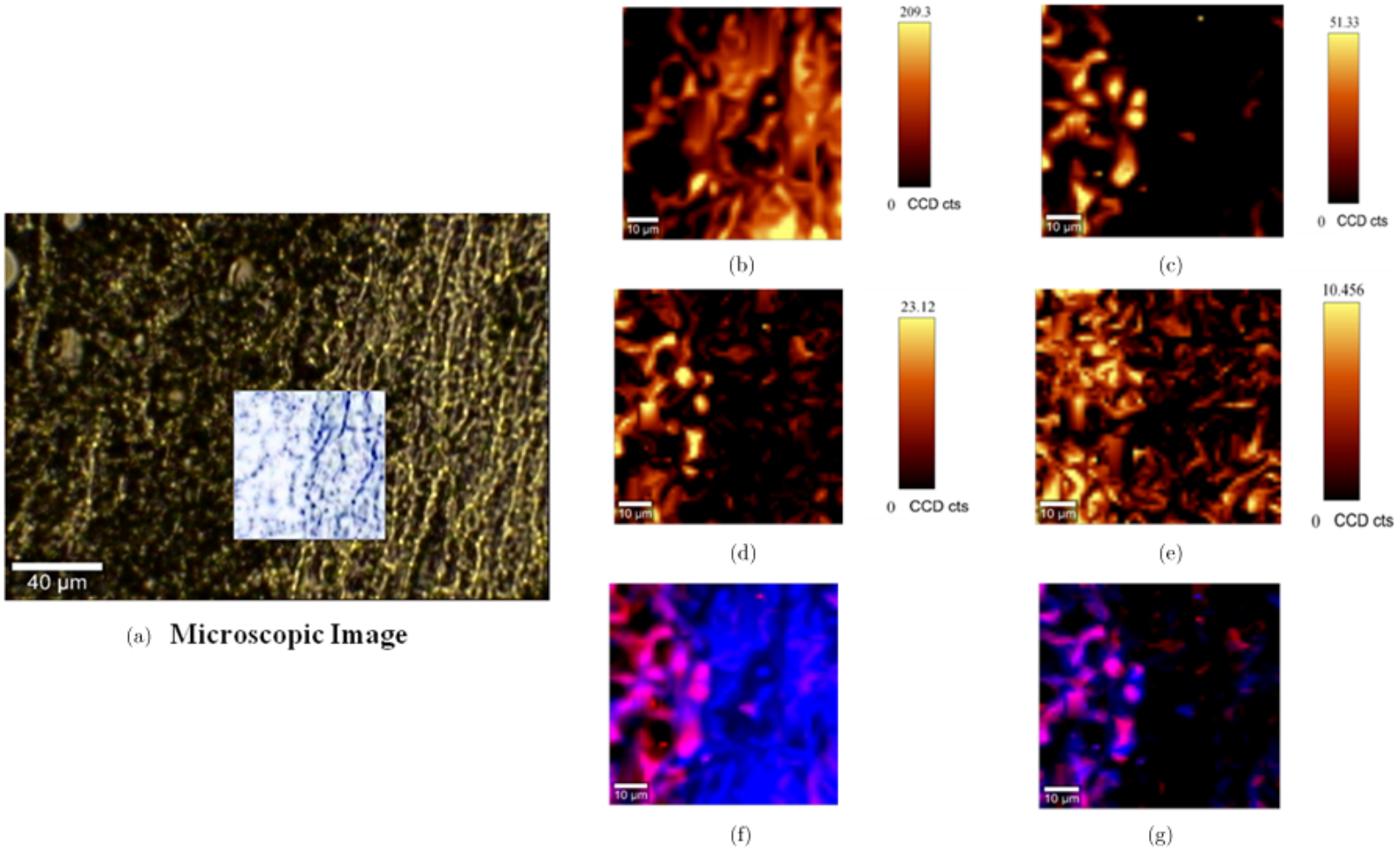

Fig. 4. The microspectral image of mouse spinal cord tissue. The microscopic image of mouse spinal cord tissue with 40 μm scale bar (a); the shadow area in image (a) represented the spectral scanning area with 10 μm scale bar. Raman images (80×60 pixels in $80 \times 60\,\mu m^2$ area) of lipid (b), protein (c), saccharides (d) and tyrosine (e) were generated by the integration of their marker bands. Image (f) shows the combined image of protein (red) and lipid (blue); image (g) shows the combined image of saccharides (red) and protein (blue).

may take place and be necessary for the establishment and maintenance of the appropriate connections between sensory fibers and their targeted cells.

Moreover, as one of the 22 amino acids that are used by cells to synthesize proteins, tyrosine exhibited a special distribution pattern in Fig. 4(e), which could attribute to two common assignments of 643 cm^{-1} Raman peak. These two assignments are usually considered as the C–C twisting mode in tyrosine, specifically within the phenol side group, and the C–S stretching mode in sulfotyrosine.[20,29,30] If the band is correctly assigned to C–S stretching, it behaves as an outcome of protein tyrosine sulfation, which carried out on a variety of secreted and intra-membrane proteins.[31] Protein tyrosine sulfation largely serves to strengthen and thereby control the interaction between secreted proteins and pathogens during the innate immune response.[32,33] If so, that explains why tyrosine exhibited an accumulation pattern in the gray matter area, but its pixel intensity is lower than protein composition as depicted by a comparable scale value. On the other side, if the band assigned to C–C stretching in tyrosine, the spectral activity of the phenol side groups is highly sensitive to the orientation of its tyrosine residue.[20] So, as shown in Fig. 4(e), a certain amount of tyrosine is spread over white matter area; meanwhile, its pixel intensity is lower than that in gray matter, which is due to the conformational/compositional change caused by tyrosine orientation variation.

4. Conclusion

All the reported data depicted the underlying common biochemical make-up of the healthy spinal cord tissue. By using multivariate and univariate methods, such as K-mean cluster analysis and chemical imaging, the featured spectral peaks can be identified clearly and the heterogeneous distribution of the substance can also be identified, which is valuable for well characterizing the biochemical specificity of tissue. Based on these advantages, the white and gray matter of the spinal cord in a mouse model is well differentiated and analyzed with microscopic Raman spectral imaging. The detailed information obtained in this study is important for interpreting the biochemical constitution of mouse spinal cord tissue, as well as the physical basis of spinal-cord-related pathological variations.

Acknowledgments

This work was supported by Natural Science Foundation of China (No. 11404258), Scientific Research Project of Education Department of Shaanxi, China (No. 14JK1743), Key Scientific Research Project of Education Department of Shaanxi, China (No. 15JS102), and Major Fundamental Research Program of Shaanxi Province, China (No. 2016ZDJC-15). This wok was also supported by the outstanding youth scholar project of Northwest University, Shaanxi, China.

References

1. B. Davey, T. Halliday, M. Hirst, *Human Biology and Health: An Evolutionary Approach*, Open University Publishing, Buckingham, UK (2001).
2. L. Marshall, J. F. Brandt, L. E. Marston, K. Ruder, "Degeneration and regeneration of axons in the lesioned spinal cord," *Physiol. Rev.* **76**(2), 319–370 (1996).
3. G. Ju, J. Wang, Y. Wang, X. Zhao, "Spinal cord contusio," *Neural. Regen. Res.* **9**(8), 789–794 (2014).
4. X. Zheng, C. Zong, M. Xu, X. Wang, B. Ren, "Raman imaging from microscopy to nanoscopy, and to macroscopy," *Small* **11**(28), 3395–3406 (2015).
5. K. A. Antonio, Z. D. Schultz, "Advances in biomedical Raman microscopy," *Anal. Chem.* **86**(1), 30–46 (2014).
6. K. Klein, A. M. Gigler, T. Aschenbrenner, R. Monetti, W. Bunk, F. Jamitzky, G. Morfill, R. W. Stark, J. Schlegel, "Label-free live-cell imaging with confocal Raman microscopy," *Biophys. J.* **102**(2), 360–368 (2012).
7. T. Saxena, B. Deng, D. Stelzner, J. Hasenwinkel, J. Chaiken, "Raman spectroscopic investigation of spinal cord injury in a rat model," *J. Biomed. Opt.* **16**(2), 027003 (2011).
8. S. Ruberto, "Raman spectroscopic investigation of chondroitinase ABC treatment after spinal cord injury in an organotypic model," Syracuse University (2013).
9. R. Galli, O. Uckermann, M. J. Winterhalder, K. H. Sitoci-Ficici, K. D. Geiger, E. Koch, G. Schackert, A. Zumbusch, G. Steiner, M. Kirsch, "Vibrational spectroscopic imaging and multiphoton microscopy of spinal cord injury," *Anal. Chem.* **84**(20), 8707–8714 (2012).
10. R. Galli, S. Tamosaityte, M. Koch, K. H. Sitoci-Ficici, R. Later, O. Uckermann, R. Beiermeister, M. Gelinsky, G. Schackert, M. Kirsch, E. Koch, G. Steiner, "Raman-based imaging uncovers the effects of alginate hydrogel implants in spinal cord injury," *Proc. of SPIE-OSA*, Vol. 9536, 95360Y (2015).

11. Y. Shi, D. Zhang, T. B. Huff, X. Wang, R. Shi, X. M. Xu, J. X. Cheng, "Longitudinal *in vivo* coherent anti-Stokes Raman scattering imaging of demyelination and remyelination in injured spinal cord," *J. Biomed. Opt.* **16**(10), 106012 (2011).
12. M. Hedegaard, C. Matthäus, S. Hassing, C. Krafft, M. Diem, J. Popp, "Spectral unmixing and clustering algorithms for assessment of single cells by Raman microscopic imaging," *Theoret. Chem. Acc.* **130**(4–6), 1249–1260 (2011).
13. Y. Mor, A. Lev-Tov, "Analysis of rhythmic patterns produced by spinal neural networks," *J. Neurophysiol.* **98**(5), 2807–2817 (2007).
14. C. Krafft, L. Neudert, T. Simat, R. Salzer, "Near infrared Raman spectra of human brain lipids," *Spectrochim. Acta A Mol. Biomol. Spectrosc.* **61**(7), 1529–1535 (2005).
15. J. Shen, L. Fan, J. Yang, A. G. Shen, J. M. Hu, "A longitudinal Raman microspectroscopic study of osteoporosis induced by spinal cord injury," *Osteoporos Int.* **21**(1), 81–87 (2010).
16. S. Wang, Z. Liang, Y. Gong, Y. Yin, K. Wang, Q. He, Z. Wang, J. Bai, "Confocal raman microspectral imaging of *ex vivo* human spinal cord tissue," *J. Photochem. Photobiol. B Biol.* **163**, 177–184 (2016).
17. K. Kochan, K. M. Marzec, K. Chruszcz-Lipska, A. Jasztal, E. Maslak, H. Musiolik, S. Chlopicki, M. Baranska, "Pathological changes in the biochemical profile of the liver in atherosclerosis and diabetes assessed by Raman spectroscopy," *Analyst* **138**(14), 3885–3890 (2013).
18. L. Vitellaro-Zuccarello, P. Bosisio, S. Mazzetti, C. Monti, S. De Biasi, "Differential expression of several molecules of the extracellular matrix in functionally and developmentally distinct regions of rat spinal cord," *Cell Tissue Res.* **327**(3), 433–447 (2007).
19. A. Rygula, K. Majzner, K. M. Marzec, A. Kaczor, M. Pilarczyk, M. Baranska, "Raman spectroscopy of proteins: A review," *J. Raman Spectrosc.* **44**(8), 1061–1076 (2013).
20. T. Masamichi, E. Yoshiko, A. Misako, S. Mika, Y. Abliz, U. Koichi, U. Tototoshi, "Raman scattering tensors of tyrosine," *Biospectroscopy* **4**, 61–71 (1998).
21. A. D. Meade, C. Clarke, F. Draux, G. D. Sockalingum, M. Manfait, F. M. Lyng, H. J. Byrne, "Studies of chemical fixation effects in human cell lines using Raman microspectroscopy," *Anal. Bioanal. Chem.* **396**(5), 1781–1791 (2010).
22. N. L. Martirosyan, J. S. Feuerstein, N. Theodore, D. D. Cacalcanti, R. F. Spetzler, M. C. Preul, "Blood supply and vascular reactivity of the spinal cord under normal and pathological conditions," *J. Neurosurg. Spine* **15**(3), 238–251 (2011).
23. P. Biglioli, M. Roberto, A. Cannata, A. Parolari, A. Fumero, F. Grillo, M. Maggioni, G. Coggi, R. Spirito, "Upper and lower spinal cord blood supply: The continuity of the anterior spinal artery and the relevance of the lumbar arteries," *J. Thorac. Cardiovasc. Surg.* **127**(4), 1188–1192 (2004).
24. K. E. Shafer-Peltier, A. S. Haka, J. T. Motz, M. Fitzmaurice, R. R. Dasari, M. S. Feld, "Model-based biological Raman spectral imaging," *J. Cell Biochem. Suppl.* **39**, 125–137 (2002).
25. N. Amharref, A. Beljebbar, S. Dukic, L. Venteo, L. Schneider, M. Pluot, M. Manfait, "Discriminating healthy from tumor and necrosis tissue in rat brain tissue samples by Raman spectral imaging," *Biochim. Biophys. Acta* **1768**(10), 2605–2615 (2007).
26. P. Morell, R. H. Quarles, "Myelin formation, structure and biochemistry," Chap. 4, G. J. Siegel, B. W. Agranoff, R. W. Albers, *et al.*, Eds., *Basic Neurochemistry: Molecular, Cellular and Medical Aspects*, 6th edition, Philadelphia (1999).
27. G. J. Siegel, R. W. Albers, S. T. Brrady, D. L. Price, *Basic Neurochemistry: Molecular, Cellular, and Medical Aspects* (Elsevier Academic Publishing, America, 2006).
28. H. Wang, Y. Fu, P. Zickmund, R. Shi, J. X. Cheng, "Coherent anti-stokes Raman scattering imaging of axonal myelin in live spinal tissues," *Biophys. J.* **89**(1), 581–591 (2005).
29. J. W. Chan, D. S. Taylor, T. Zwerdling, S. M. Lane, K. Ihara, T. Huser, "Micro-Raman spectroscopy detects individual neoplastic and normal hematopoietic cells," *Biophys. J.* **90**(2), 648–656 (2006).
30. N. Stone, M. C. Hart Prito, P. Crow, J. Uff, A. W. Ritchie, "The use of Raman spectroscopy to provide an estimation of the gross biochemistry associated with urological pathologies," *Anal. Bioanal. Chem.* **387**(5), 1657–1668 (2007).
31. K. L. Moore, "Protein tyrosine sulfation: A critical posttranslation modification in plants and animals," *Proc. Natl Acad. Sci. USA* **106**(35), 14741–14742 (2009).
32. I. Spitzbarth, P. Bock, V. Haist, V. M. Stein, A. Tipold, K. Wewetzer, W. Baumgärtner, A. Beineke, "Prominent microglial activation in the early proinflammatory immune response in naturally occurring canine spinal cord injury," *J. Neuropathol. Exp. Neurol.* **70**(8), 703–714 (2011).
33. S. A. Fox, A. A. Shanblatt, H. Beckman, J. Strasswimmer, A. C. Terentis, "Raman spectroscopy differentiates squamous cell carcinoma (SCC) from normal skin following treatment with a high-powered CO2 laser," *Lasers Surg. Med.* **46**(10), 757–772 (2014).